A compact and closed-loop spin-exchange relaxation-free atomic magnetometer for wearable magnetoencephalography

Qing-Qian Guo(郭清乾)[1,2,3], Tao Hu(胡涛)[1,3,†], Xiao-Yu Feng(冯晓宇)[3], Ming-Kang Zhang(张明康)[4], Chun-Qiao Chen(陈春巧)[4], Xin Zhang(张欣)[1,2,3], Ze-Kun Yao(姚泽坤)[4], Jia-Yu Xu(徐佳玉)[4], Qing Wang(王青)[1,2,3], Fang-Yue Fu(付方跃)[4], Yin Zhang(张寅)[1,3], Yan Chang(常严)[1,3], and Xiao-Dong Yang(杨晓冬)[3,1,‡]

[1] *Suzhou Institute of Biomedical Engineering and Technology, Chinese Academy of Sciences, Suzhou* 215163, *China*
[2] *School of Biomedical Engineering (Suzhou), Division of Life Sciences and Medicine, University of Science and Technology of China, Hefei* 230026, *China*
[3] *Jihua Laboratory, Foshan* 528000, *China*
[4] *School of Electronic and Information Engineering, Changchun University of Science and Technology, Changchun* 130022, *China*

(Received 3 May 2022; revised manuscript received 24 June 2022; accepted manuscript online 5 July 2022)

Atomic magnetometers operated in the spin-exchange relaxation-free (SERF) regime are the promising sensor to replace superconducting quantum interference devices (SQUIDs) in the biomagnetism field. The SERF magnetometer with compact size and good performance is crucial to the new generation of wearable magnetoencephalography (MEG) system. In this paper, we developed a compact and closed-loop SERF magnetometer with the dimensions of 15.0×22.0×30.0 mm^3 based on a single-beam configuration. The bandwidth of the magnetometer was extended to 675 Hz while the sensitivity was maintained at 22 fT/Hz$^{1/2}$. A nearly 3-fold enhancement of the bandwidth was obtained in comparison with the open-loop control. The implementation of the closed-loop control also greatly improved the dynamic range, enabling the magnetometer to be robust against the disturbance of the ambient field. Moreover, the magnetometer was successfully applied for the detection of human α-rhythm and auditory evoked fields (AEFs), which demonstrated the potential to be extended to multi-channel MEG measurements for future neuroscience studies.

Keywords: atomic magnetometer, miniaturization, closed-loop, magnetoencephalography (MEG)

PACS: 07.55.Ge, 07.07.Df, 87.85.–d, 87.85.Pq **DOI:** 10.1088/1674-1056/ac7e38

1. Introduction

Magnetoencephalography (MEG) is a promising and non-invasive neuroimaging technique for recording brain electrophysiological activities, providing millisecond temporal resolution and millimeter spatial tracking of brain activation signatures.[1,2] The traditional MEG device employs an array of superconducting quantum interference devices (SQUIDs) around the head.[3] However, the requirement of cryogenic cooling increases the distance between the scalp and sensor at least few centimeters (2–6 cm) and reduces the detection signal-to-noise ratio (SNR).[4] Furthermore, the fixed sensor geometry of the SQUID-based MEG system limits the participant movement, which makes some paradigms requiring large head movements cannot be performed.[5] Compared with the SQUID, the spin-exchange relaxation-free (SERF) atomic magnetometers with intrinsic advantages of non-cryogenic feature, low-cost, miniaturization, and closer detecting distance ($<$ 1 cm) have been developed to realize flexible and wearable MEG measurements which enable subjects to be free to move and interact with the real world across all ages and patient groups.[6–8] Moreover, a series of studies have demonstrated clear improvements in SNR and tracking accuracy of atomic magnetometer-based MEG due to the closer detecting distance.[9,10]

The classical SERF magnetometers are usually designed in the two-beam (pump-probe) configuration, which is based on the Faraday effect detection.[11–13] This configuration has the higher sensitivity,[14] however, it is difficult to be integrated into a miniature sensor head due to the quite complicated optical path. In contrast, the single-beam configuration greatly simplified the optical structure, allowing its volume to be much smaller than the two-beam configuration and enabling the multi-channel MEG detection.[10,15] Liu *et al.* proposed a compact single-beam magnetometer with a bandwidth of 125 Hz, while the sensitivity was maintained at 30 fT/Hz$^{1/2}$.[16] Zhang *et al.* reported an integrated VCSEL-based magnetometer with a sensitivity of 35 fT/Hz$^{1/2}$ and successfully recorded the magnetocardiography (MCG) signals.[17] Du *et al.* proposed a miniature four-channel magnetometer with a sensitivity of 6 fT/Hz$^{1/2}$ in a gradiometer arrangement and demonstrated the feasibility of using the magnetometer for MEG recordings.[18] Furthermore, the existing commercial compact SERF magnetometer (QZFM, QuSpin Inc) is also designed in the single-beam configuration, which has 10 fT/Hz$^{1/2}$ sensitivity.[19] The new generation of wearable MEG system has been successfully developed by using

†Corresponding author. E-mail: hutao@sibet.ac.cn
‡Corresponding author. E-mail: xiaodong.yang@sibet.ac.cn

© 2023 Chinese Physical Society and IOP Publishing Ltd

the commercial magnetometers.[20–22] Although the sensitivity of the commercial magnetometer is excellent, this comes at the cost of narrow bandwidth ($\sim$ 100 Hz) and operation in a low dynamic range ($\pm$1.5 nT). The narrow bandwidth will hinder the applications in some MEG cases with the requirement of a much broader frequency range.[23,24] For example, in the field of epilepsy, which is associated with high frequency ($>$ 100 Hz) oscillations (HFOs), has received much attention as being possible biomarkers of epileptogenic brain tissue.[25] The low dynamic range will limit the subjects' movement for wearable MEG measurements, which need extra field-nulling coils system.[26] Therefore, it is crucial to develop a compact SERF magnetometer with high sensitivity, high bandwidth and high dynamic range to expand the applications.

In this work, we developed a proportional-integral (PI) controller-based closed-loop and compact SERF magnetometer with single-beam configuration. Compared with the open-loop control, the bandwidth of the magnetometer was extended to 675 Hz and a flat-response was obtained up to 300 Hz while the sensitivity was maintained at 22 fT/Hz$^{1/2}$. The dynamic range has also been greatly improved and effectively reduces the requirement of the shielding environment. Moreover, the designed magnetometer was successfully applied on human α-rhythm and auditory evoked fields (AEFs) measurement, which demonstrated the promising potential for future multi-channel MEG system.

2. Experimental setup

The schematic diagram of the close-loop atomic magnetometer is shown in Fig. 1(a). A 4×4×4 mm^3 cubical atomic vapor cell (inner length is 3 mm) contained a droplet rubidium (^{87}Rb) alkali-metal and 700 Torr N_2 as the quenching and buffering gas for slowing down Rb atoms collision relaxation rate from the cell wall. The center of the vapor cell was designed to be 6.5 mm away from the front part of the sensor head. To achieve sufficient Rb atoms density, the vapor cell was electrically heated to around 140 °C with two non-magnetic heaters driven by a 20 kHz AC. The aerogel was used as thermal insulation to minimize heat loss and ensure the temperature outside the sensor was below 40 °C. The temperature of the cell was stabilized at 0.1 °C level by applying a feedback system. A set of three-axis magnetic field coils wrapped around the vapor cell for compensating the external magnetic field and applying the modulation field. The assembled prototype of the compact magnetometer sensor is shown in Fig. 1(b) and the outside dimension is only 15.0×22.0×30.0 mm^3.

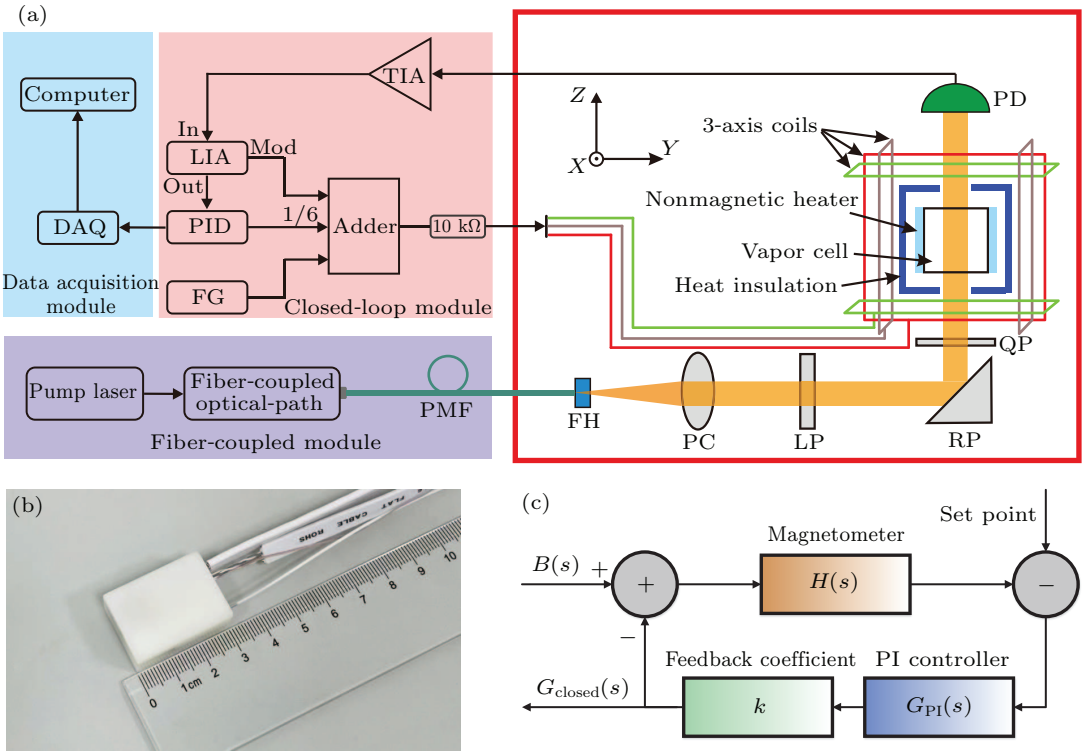


Fig. 1. (a) Schematic diagram of the compact magnetometer; PMF: polarization maintaining fiber; FH: fiber holder; PC: plano-convex lens; LP: linear polarizer; RP: reflecting prism; QP: quarter-wave plate; PD: photodiode; TIA: trans-impedance amplifier; LIA: lock-in amplifier; FG: function generator; DAQ: data acquisition. (b) Photograph of the assembled sensor head. The external dimensions are 15.0×22.0×30.0 mm^3. (c) The block diagram of the closed-loop system.

A 795 nm distributed Bragg reflector (DBR) laser resonant with the D1 line of ^{87}Rb for optical pumping was coupled into a single-mode polarization-maintaining fiber (PMF), which was fixed at the entrance of the sensor package. The laser beam was collimated with a plano-convex lens, and then passed through the linear polarizer, prism, and quarter-

wave plate to form a circularly polarized light. After passing through the center of the vapor cell along the z-axis, the transmitted light was detected by a photoelectric detector (PD). The output signal of PD was A/V converted by a trans-impedance amplifier (TIA) and demodulated by the lock-in amplifier. For the closed-loop control system, the demodulated output of the lock-in amplifier was fed to the analog proportional-integral-derivative (PID) controller whose output was used to compensate the magnetic field around the vapor cell to zero in the measuring direction (y-direction). The feedback signal was multiplied by a factor of $1/6$ to minimize the electronic noise generated by the PID controller and applied to the coils with a 10 kΩ resistance. Meanwhile, the feedback signal was also detected by the data acquisition card.

3. Theoretical analysis

The behavior of the electron spin can be modeled by the density-matrix equation (DME). The SERF magnetometer should operate in a low magnetic field and high alkali-metal density and the spin-exchange rate is much faster than the rate of the Larmor precession. As a result, the electron spin polarization can be phenomenologically described by the Bloch equation[27,28]

$$\frac{\mathrm{d}\boldsymbol{P}}{\mathrm{d}t} = D\nabla^2\boldsymbol{P} + \frac{1}{q}\left[\gamma_{\mathrm{e}}\boldsymbol{B}\times\boldsymbol{P} + R_{\mathrm{op}}(\hat{z}-\boldsymbol{P}) - R_{\mathrm{rel}}\boldsymbol{P}\right], \quad (1)$$

where D is the diffusion constant and can be ignored in the high-pressure buffer gas. $\boldsymbol{P}$ is the electron spin polarization, $\boldsymbol{B}$ is the external magnetic field, γ_{e} is the gyromagnetic ratio of the electron, q is the nuclear slowing down factor, R_{op} is the optical pumping rate, z is defined by the direction of the laser beam and R_{rel} is the total spin relaxation rate. The second term on the right side of Eq. (1) depicts the spin precession in the magnetic field, the third term describes the effect of optical pumping to polarize the spin along z direction, and the last term describes the effect of spin relaxation to depolarize the spin.

To achieve the zero-field magnetic resonance for sensitive measurement of the magnetic field along the y-direction, the x, y and z components of the magnetic field were first compensated less than 0.1 nT. In the presence of a slowly changing magnetic field along the y-direction (B_y), the transverse polarization (P_{zx}) can be substituted by utilizing a complex notation $P_{zx} = P_z + \mathrm{i}P_x$. Thus, the Bloch equation can be simplified as

$$\frac{\mathrm{d}P_{zx}}{\mathrm{d}t} = \frac{P_0 - P_{zx}}{\tau} - \frac{\mathrm{i}\gamma_{\mathrm{e}}(P_{zx}B_y)}{q}, \quad (2)$$

where $P_0 = R_{\mathrm{op}}/(R_{\mathrm{op}}+R_{\mathrm{rel}})$, $1/\tau = R_{\mathrm{op}}+R_{\mathrm{rel}}$. In the case of a modulation field ($B_{\mathrm{m}} = B_1\cos\omega\mathrm{t}$) applied along the y direction, the Eq. (2) can be expressed as

$$\frac{\mathrm{d}P_{zx}}{\mathrm{d}t} = \frac{P_0 - P_{zx}}{\tau} - \frac{\mathrm{i}\gamma_{\mathrm{e}}P_{zx}(B_y + B_1\cos\omega t)}{q}. \quad (3)$$

The dominant term of the solution (Eq. (3)) is the first harmonic component of the spin polarization, which can be described as[29,30]

$$P_z = \frac{P_0\omega_0\tau}{1+(\omega_0\tau)^2}J_0\left(\frac{\omega_1}{\omega}\right)J_1\left(\frac{\omega_1}{\omega}\right)\sin\omega t, \quad (4)$$

where $\omega_0 = \gamma_{\mathrm{e}}\cdot B_y/q$ and $\omega_1 = \gamma_{\mathrm{e}}\cdot B_1/q$ which describe the Larmor precession rate in the external magnetic field of B_y and modulate magnetic field (B_1). J_0 and J_1 are the Bessel functions of first kind with the order 0 and 1, respectively. Due to the amplitude-modulation, the B_y field signal is shifted away from the low-frequency band and synchronously demodulated by a lock-in amplifier, which effectively suppresses the low-frequency noise. Furthermore, the output of the lock-in amplifier expresses as a dispersion curve shape with the B_y field and the central linear portion of this curve as the dynamic range is used for magnetic field detection.

For the open-loop operation, the response of the magnetometer can be modeled as a first-order low pass filter[12] and the transfer function can be expressed as (Fig. 1(c))

$$H(s) = \frac{G_{\mathrm{open}}(s)}{B(s)} = \frac{G_0\omega_{\mathrm{c}}}{s+\omega_{\mathrm{c}}}, \quad (5)$$

where the G_0 is the DC gain, ω_{c} is the cut-off frequency and the variable has the form $s = \mathrm{j}\omega$. To improve the performance of the magnetometer, a PI controller-based closed-loop operation mode is developed. The transfer function of the PI controller has the form as

$$G_{\mathrm{PI}} = K_{\mathrm{p}}\left(1+\frac{K_{\mathrm{I}}}{s}\right), \quad (6)$$

where K_{p} and K_{I} are the proportion and integral coefficients of PI controller, respectively. The setpoint was set to zero. In the closed-loop system, the output of the PI controller is fed back to the y-axis coil to lock the magnetic field along the sensitive axis (y-axis) to zero. According to the block diagram (Fig. 1(c)), the closed-loop transfer function can be written as[11]

$$\begin{aligned} H_{\mathrm{closed}}(s) &= \frac{G_{\mathrm{closed}}(s)}{B(s)} = \frac{kH(s)G_{\mathrm{PI}}(s)}{kH(s)G_{\mathrm{PI}}(s)+1} \\ &= \frac{kG_0K_{\mathrm{p}}\omega_{\mathrm{c}}(s+K_{\mathrm{I}})}{s^2+(kG_0K_{\mathrm{p}})s\omega_{\mathrm{c}}+kG_0K_{\mathrm{p}}K_{\mathrm{I}}\omega_{\mathrm{c}}}, \end{aligned} \quad (7)$$

where k is the feedback coefficient. The Eq. (7) indicates that the frequency response of the closed-loop magnetometer will approach 1 by tuning the $G_{\mathrm{PI}}(s)$ to a large value ($kH(s)G_{\mathrm{PI}}(s) \gg 1$). It means that the closed-loop magnetometer is free from amplitude attenuation for measuring magnetic signals. As a result, the closed-loop magnetometer provides a convenient way to get a flat response over a wide frequency range, which is beneficial to improve the bandwidth.

4. Results and discussion

4.1. Sensor characterization

The performance of the designed magnetometer was characterized in a five-layer, 20-cm inner diameter cylindrical mu-metal shielding with a residual magnetic field of less than 1 nT. In the closed-loop system, the values of K_{p} and K_{I} were set as -0.7 and 700 s^{-1}, respectively. Figure 2(a) shows the normalized frequency responses of the open-loop (blue curve) and closed-loop (pink curve) magnetometers, which were obtained by sweeping the frequency of a small constant field along the y-axis and measuring the corresponding output amplitude. The open-loop amplitude-frequency response curve falls rapidly from 40 Hz, which leads to a narrow -3 dB bandwidth of 240 Hz. In the closed-loop magnetometer, a more flat-response is obtained up to 300 Hz and the -3 dB bandwidth is expanded to 675 Hz, which is about 3 times improvement compared to the open-loop magnetometer. Furthermore, the effect of K_{p} and K_{I} for the normalized amplitude-frequency responses and bandwidth of the closed-loop magnetometer is discussed in the supplemental material.

The noise-limited magnetic-field sensitivity for the open-loop magnetometer ($S_{\mathrm{open-loop}}$) and closed-loop magnetometer ($S_{\mathrm{closed-loop}}$) can be respectively expressed as

$$S_{\mathrm{open-loop}} = \frac{G_0\,(\mathrm{nT/V})\cdot V_{\mathrm{open}}\left(\mathrm{V/Hz^{1/2}}\right)}{FR_{\mathrm{open}}}, \tag{8}$$

$$\begin{aligned} S_{\mathrm{closed-loop}} &= \frac{102\,(\mathrm{nT/mA})}{6\times 10\,(\mathrm{k\Omega})}\cdot\frac{V_{\mathrm{PI}}\left(\mathrm{V/Hz^{1/2}}\right)}{FR_{\mathrm{closed}}} \\ &= \frac{k\,(\mathrm{nT/V})\times V_{\mathrm{PI}}\left(\mathrm{V/Hz^{1/2}}\right)}{FR_{\mathrm{closed}}}, \end{aligned} \tag{9}$$

where V_{open} and V_{PI} represent the voltage noise power spectral density of the open-loop output and the PI controller feedback, respectively. G_0 is the DC response of the open-loop magnetometer of 1.13 nT/V. FR_{open} and FR_{closed} represent the normalized amplitude-frequency responses of the open-loop and closed-loop magnetometers (Fig. 2(a)), respectively. 102 nT/mA is the coil constant of the y-direction coil and k is the feedback coefficient (1.7 nT/V). Moreover, to characterize the noise-limited magnetic-field sensitivity of the magnetometer, we applied a small oscillating field with an amplitude of 102 pT at the frequency of 30 Hz. As can be seen from Fig. 2(b), the sensitivity of open-loop magnetometer is consistent with the closed-loop magnetometer within 180 Hz. With the increase of frequency, the open-loop sensitivity is gradually deteriorated from 22fT/$\mathrm{Hz^{1/2}}$ to 60 fT/$\mathrm{Hz^{1/2}}$ (180–700 Hz) due to the decline of frequency response. For the closed-loop control, the sensitivity is kept around 22 fT/$\mathrm{Hz^{1/2}}$ in a large range of 30 Hz to 400 Hz. Compared with the open-loop control, the sensitivity can be improved less than 30 fT/$\mathrm{Hz^{1/2}}$ in the higher frequency range (400 Hz to 700 Hz). In addition, we also evaluated the photon shot noise (13 fT/$\mathrm{Hz^{1/2}}$) and modulation magnetic noise (17 fT/$\mathrm{Hz^{1/2}}$), which mainly limit the further improvement of the sensitivity.

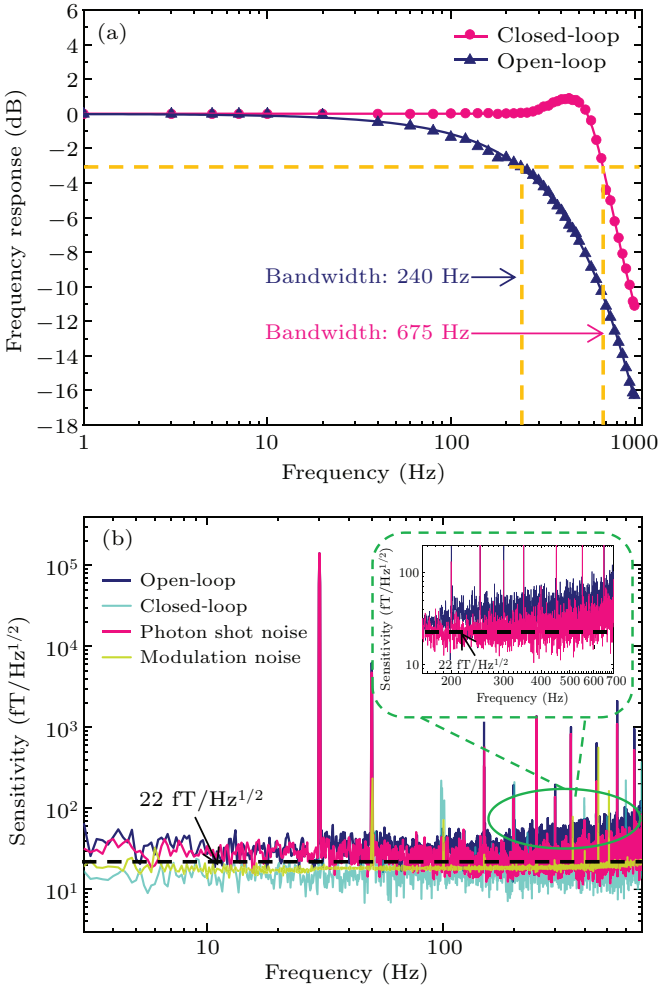


Fig. 2. (a) The normalized amplitude-frequency responses of the open-loop (blue curve) and closed-loop (pink curve) magnetometers. (b) The noise-limited magnetic-field sensitivity of the two magnetometers.

The dynamic range is also an important parameter of the atomic magnetometer, which influences the working environment in practical application. A magnetic field swept from -15 nT to $+15$ nT is applied to evaluate the dynamic range of the designed magnetometer. As shown in Fig. 3, to calculate the open-loop dynamic range (blue curve), the magnetometer response was linear fitted around the 0 nT, and the fitted result indicates that the linear response was limited at the range of ± 2.5 nT with the nonlinear error of less than 1%. In the closed-loop system, the magnetic field around the vapor cell was locked to zero by PI feedback. Therefore, the dynamic range of the magnetometer will not be affected by the dispersion curve, which enables a linear response in the whole magnetic field range (pink curve). Compared with the open-loop control, the dynamic range is increased by a factor of 6

through the implementation of closed-loop control. Furthermore, according to Eq. (9), the dynamic range is only limited by the feedback coefficient and can be further improved by reducing the connective resistance or increasing the coil constant. The wide dynamic range can effectively resist the fluctuation of residual magnetism especially for the moving MEG measurement and reduce the requirement of the magnetically shielded room.

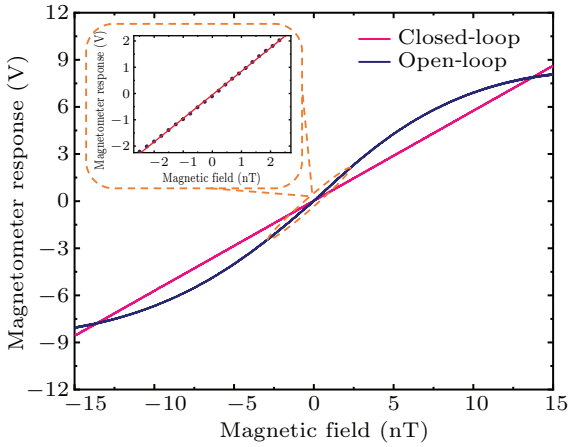


Fig. 3. The magnetometer response of the sweeping magnetic field from −15 nT to +15 nT. The inset shows the linear range of the open-loop response is ±2.5nT.

4.2. MEG experiments

Human α-rhythm photic blocking and auditory evoked response experiments were carried out to demonstrate the designed magnetometer's feasibility for MEG measurement. All the MEG experiments were conducted in the magnetically shielded room (MSR) with an internal dimension of $1.75\times1.95\times2.23$ m^3 (Fig. 4(a)) and a noise level less than 15 fT/Hz$^{1/2}$ (No. 710 R&D Institute, CSIC, Yichang, China). This study was approved by the Suzhou Institute of Biomedical Engineering and Technology Research Ethic Committee and all participants provided written informed consent. For the detection of α-rhythm (8–13 Hz) signal, the spontaneous MEG was recorded with the magnetometer positioned over the occipital cortex by a nonmagnetic mount (Fig. 4(b)). The subject was instructed via a home-made brain function stimulation device (Fig. 4(c)) and an air duct earphone in a bright environment. During the α-rhythm experiment, the subject was asked to keep eyes open in the initial waiting time for about 10 s, and followed by a series of alternating periods of 10 s eyes closed and 5 s eyes open (Fig. 4(d)). Through the processing of 6.5–13.5 Hz bandpass filter, periodic amplitude variations of the α-rhythm MEG signal was shown in Fig. 4(e). The gray and yellow blocks represent the states of eyes open and closed, respectively. When the subject opened eyes, the α-rhythm was attenuated and the amplitude was substantially reduced. The short-time Fourier transform (STFT) spectrum (Fig. 4(f)) also clearly revealed the α-rhythm oscillations located at about 9–12 Hz with an interval of 5 s (open eyes).

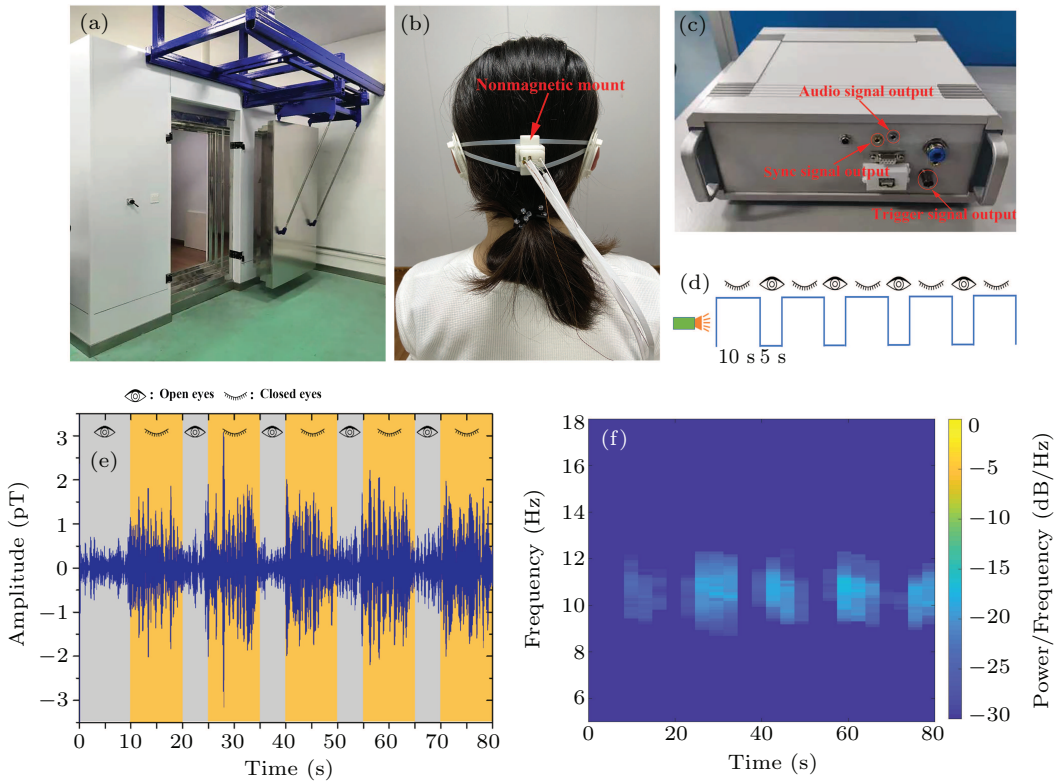


Fig. 4. (a) The magnetically shielded room with a noise level less than 15 fT/Hz$^{1/2}$. (b) Photograph of the magnetometer positioned over occipital cortex for detecting the α-rhythm signal. (c) The home-made brain function stimulation device. (d) Experimental design of α-rhythm detection. (e) The time-domain α-rhythm MEG signal. (f) The short-time Fourier transform spectrum of the α-rhythm MEG signal.

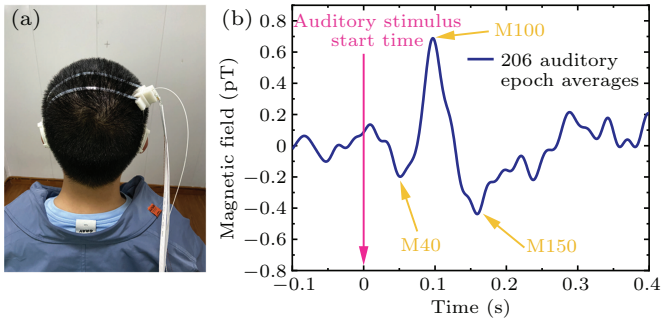


Fig. 5. (a) Photograph of the magnetometer positioned over right temporal lobe for detecting the auditory evoked field signal. (b) Auditory evoked field signal detected with the magnetometer.

For measuring the human auditory evoked fields (AEFs), we provided 1 kHz auditory stimuli with a duration of 300 ms. The stimuli were mixed with randomized 1.2 kHz auditory stimuli (300 ms) to prevent subject adaptation. The time interval between each stimulus is distributed immutably at 1.7 s. The subject wore the air duct earphone by left ear to hear the sound from the stimulation device. The magnetometer was located near the right temporal lobe (auditory cortex) region during the experiment. The measured MEG data corresponding to the 1 kHz stimuli was extracted by referring to the trigger signal. Subsequently, the extracted data was bandpass filtered (2–45 Hz) and averaged over all 1 kHz stimuli. The AEF signal can be clearly observed in Fig. 5(b). The earliest response, M40, about 40 ms after the stimulus onset, was followed by a prominent deflection in the opposite direction at about 100 ms (M100) and by another response peak at 150 ms (M150).

5. Conclusion

We developed a compact and closed-loop SERF magnetometer with the dimensions of $15.0\times22.0\times30.0$ mm^3 and experimentally demonstrated the feasibility for the detection of MEG signal. Compared with the open-loop control, the bandwidth of the closed-loop magnetometer can approach to 675 Hz, while the sensitivity has remained at 22 fT/Hz$^{1/2}$ in the frequency range of 30–400 Hz. The dynamic range has also been greatly improved to ±15 nT, which enables the magnetometer to be robust against the disturbance of the ambient field. Furthermore, the high SNR α-rhythm and auditory evoked field signal were successfully detected by the designed magnetometer. The results show that the developed compact magnetometer has the potential to be extended to multi-channel arrays, which provide a promising application in the new generation wearable MEG system.

Acknowledgements

Project supported by Ji Hua Laboratory (Grant No. X190131TD190), the Research and Development Project for Equipment of Chinese Academy of Sciences (Grant No. YJKYYQ20210051), the Suzhou pilot project of basic research (Grant No. SJC2021024), and the Natural Science Foundation of Jiangsu Province, China (Grant No. BK20200215).

References

[1] Cohen D 1972 *Science* **175** 664
[2] Boto E, Holmes N, Leggett J, Roberts G, Shah V, Meyer S S, Munoz L D, Mullinger K J, Tierney T M, Bestmann S, Barnes G R, Bowtell R and Brookes M J 2018 *Nature* **555** 657
[3] Hämäläinen M, Hari R, Ilmoniemi R J, Knuutila J and Lounasmaa O V 1993 *Rev. Mod. Phys.* **65** 413
[4] Boto E, Meyer S S, Shah V, Alem O, Knappe S, Kruger P, Fromhold T M, Lim M, Glover P M, Morris P G, Bowtell R, Barnes G R and Brookes M J 2017 *NeuroImage* **149** 404
[5] Roberts G, Holmes N, Alexander N, Boto E, Leggett J, Hill R M, Shah V, Rea M, Vaughan R, Maguire E A, Kessler K, Beebe S, Fromhold M, Barnes G R, Bowtell R and Brookes M J 2019 *Neuroimage* **199** 408
[6] Hill R M, Boto E, Holmes N, Hartley C, Seedat Z A, Leggett J, Roberts G, Shah V, Tierney T M, Woolrich M W, Stagg C J, Barnes G R, Bowtell R, Slater R and Brookes M J 2019 *Nat. Commun.* **10** 4785
[7] Boto E, Hill R M, Rhodes N, Osborne J, Doyle C, Holmes N, Rea M, Leggett J, Bowtell R and Brookes M J 2022 *NeuroImage* **252** 119027
[8] Tierney T M, Levy A, Barry D N, Meyer S S, Shigihara Y, Everatt M, Mellor S, Lopez J D, Bestmann S, Holmes N, Roberts G, Hill R M, Boto E, Leggett J, Shah V, Brookes M J, Bowtell R, Maguire E A and Barnes G R 2021 *Neuroimage* **225** 117443
[9] Sheng J, Wan S, Sun Y, Dou R, Guo Y, Wei K, He K, Qin J and Gao J H 2017 *Rev. Sci. Instrum.* **88** 094304
[10] Hill R M, Boto E, Rea M, Holmes N, Leggett J, Coles L A, Papastavrou M, Everton S K, Hunt B A E, Sims D, Osborne J, Shah V, Bowtell R and Brookes M J 2020 *Neuroimage* **219** 116995
[11] Guo Q Q, Hu T, Chen C Q, Feng X Y, Wu Z Y, Zhang Y, Zhang M K, Chang Y and Yang X D 2021 *IEEE Sens. J.* **21** 21425
[12] Allred J C, Lyman R N, Kornack T W and Romalis M V 2002 *Phys. Rev. Lett.* **89** 130801
[13] Ito Y, Ohnishi H, Kamada K and Kobayashi T 2011 *IEEE Trans. Magn.* **47** 3550
[14] Li J D, Quan W, Zhou B Q, Wang Z, Lu J X, Hu Z H, Liu G and Fang J C 2018 *IEEE Sens. J.* **18** 8198
[15] Mhaskar R, Knappe S and Kitching J 2012 *Appl. Phys. Lett.* **101** 241105
[16] Liu G, Tang J, Yin Y, Wang Y, Zhou B and Han B 2020 *IEEE Sens. J.* **20** 5827
[17] Zhang G, Zeng H, Tan G and Lin Q 2022 *IEEE Sens. J.* **22** 7700
[18] Du P C, Li J J, Yang S J, Wang X T, Zhuo Y, Wang F and Wang R Q 2019 *Chin. Phys B* **28** 040702
[19] Osborne J, Orton J, Alem O and Shah V 2018 *Steep Dispersion Engineering and Opto-Atomic Precision Metrology XI*, 22 February, 2018, California, United States, p. 105481G
[20] Barry D N, Tierney T M, Holmes N, Boto E, Roberts G, Leggett J, Bowtell R, Brookes M J, Barnes G R and Maguire E A 2019 *Neuroimage* **203** 116192
[21] Tierney T M, Holmes N, Meyer S S, Boto E, Roberts G, Leggett J, Buck S, Duque-Munoz L, Litvak V, Bestmann S, Baldeweg T, Bowtell R, Brookes M J and Barnes G R 2018 *Neuroimage* **181** 513
[22] Zhang X, Chen C Q, Zhang M K, Ma C Y, Zhang Y, Wang H, Guo Q Q, Hu T, Liu Z B, Chang Y, Hu K J and Yang X D 2020 *J Neurosci Methods* **346** 108948
[23] Baillet S 2017 *Nat. Neurosci.* **20** 327
[24] T Fedele H J S, M Burghoff, G Curio and R Körber 2015 *Physiol. Meas.* **36** 357
[25] Lopes da Silva F 2013 *Neuron* **80** 1112
[26] Holmes N, Leggett J, Boto E, Roberts G, Hill R M, Tierney T M, Shah V, Barnes G R, Brookes M J and Bowtell R 2018 *Neuroimage* **181** 760
[27] Ledbetter M P, Savukov I M, Acosta V M, Budker D and Romalis M V 2008 *Phys. Rev. A* **77** 033408
[28] Tang J, Yin Y, Zhai Y, Zhou B, Han B, Yang H and Liu G 2021 *Opt. Express* **29** 8333
[29] Cohen-Tannoudji C, Dupont-Roc J, Haroche S and Lalo€ E F 1970 *Rev. Phys. Appl.* **5** 95
[30] Tierney T M, Holmes N, Mellor S, Lopez J D, Roberts G, Hill R M, Boto E, Leggett J, Shah V, Brookes M J, Bowtell R and Barnes G R 2019 *NeuroImage* **199** 598